INORGANIC CHEMISTRY
FRONTIERS

RESEARCH ARTICLE

View Article Online
View Journal | View Issue

Cite this: *Inorg. Chem. Front.*, 2022, **9**, 4881

Manipulating Ru oxidation within electrospun carbon nanofibers to boost hydrogen and oxygen evolution for electrochemical overall water splitting†

Mengxiao Zhong, Su Yan, Jiaqi Xu, Ce Wang and Xiaofeng Lu *

Received 31st May 2022,
Accepted 31st July 2022

DOI: 10.1039/d2qi01168a

rsc.li/frontiers-inorganic

Developing bifunctional electrocatalysts with high efficiency and prominent durability toward overall water splitting is a fascinating way to produce hydrogen for clean energy applications. In this work, partially oxidized Ru nanoparticles integrated within electrospun carbon nanofibers (RuO_2/Ru-CNFs) are prepared *via* a convenient electrospinning–carbonization–oxidation process. Benefitting from the small size of the active nanoparticles, the formation of a RuO_2/Ru heterostructure and the introduction of a carbon substrate, the optimized RuO_2/Ru-CNFs-350 catalyst delivers excellent OER and HER performances with ultralow overpotentials of 203 mV and 21 mV at 10 mA cm^{-2}, respectively, along with remarkable long-term stabilities under alkaline conditions. Moreover, we constructed an alkaline overall water splitting electrolyzer with RuO_2/Ru-CNFs-350 as both the anode and cathode, achieving a low working voltage of 1.452 V at 10 mA cm^{-2}, superior to that of the benchmark Pt/C||RuO_2 couple (1.560 V). This work provides a convenient and promising route to fabricate high-performance bifunctional electrocatalysts toward water electrolysis.

Introduction

Due to the environmental deterioration and the increasingly serious energy crisis, the development of sustainable and clean energy is of great significance to human society.[1–4] Since John Bockris presented the term hydrogen economy in a speech at the General Motors Technology Center in 1970, hydrogen energy has captured significant attention, and thus far, it has been broadly used in industrial production, such as the synthesis of ammonia and the refining of fossil fuel.[5] Beyond that, hydrogen-powered fuel cells have shown great promise in automobiles and consumer electronics.[6] However, most hydrogen is still obtained from coal gasification or steam methane reforming, leading to the large emission of CO_2 and high energy consumption, which is contrary to the goal of carbon neutrality.[5] Electrochemical water electrolysis has attracted widespread attention for generating hydrogen because of its low-cost electricity produced by sustainable energy (solar energy, wind energy, *etc.*).[7–10] This sustainable approach solves the problem of renewable energies not being available as continuous power sources due to their intermittent nature, and achieves zero CO_2 emission throughout the process.[6,11–13] However, the practical water decomposition is found to overcome the overpotentials resulting from the hydrogen evolution reaction (HER) and oxygen evolution reaction (OER) at the cathode and anode, respectively. Therefore, the actual overpotential toward the overall water splitting is far beyond its thermodynamic potential (1.23 V), and especially the OER as the key and bottleneck-type reaction with sluggish kinetics hinders the overall efficiency.[14–16]

In recent years, many electrocatalysts have been created to reduce the energy barrier toward the OER or HER. Among them, bifunctional catalysts are highly attractive in the electrochemical water splitting field because of their distinct capability of catalyzing both the OER and HER in the same electrolyte.[17–19] Precious metal catalysts with high electrocatalytic activity are strongly limited for large-scale practical applications because of their scarcity, high cost and poor stability.[20,21] On the other hand, many non-precious metal-based catalysts have been explored to present electrocatalytic properties for overall water splitting, while their low intrinsic activity still hinders their practical usage. Thus, searching for high-efficiency and durable electrocatalysts toward overall water splitting remains highly desirable but challenging. Ruthenium dioxide (RuO_2) with a rutile phase is well known to exhibit remarkable performance in terms of the OER in both acidic and alkaline electrolytes,[22–25] but their HER activity is

Alan G. MacDiarmid Institute, College of Chemistry, Jilin University, 2699 Qianjin Street, Changchun 130012, P. R. China. E-mail: xflu@jlu.edu.cn

† Electronic supplementary information (ESI) available. See DOI: https://doi.org/10.1039/d2qi01168a

inferior. Recently, metallic ruthenium (Ru) materials have been demonstrated as promising alternatives to platinum (Pt) toward the HER because their bond strength with hydrogen is similar to that of Pt, and they are much cheaper.[26–28] Previous studies have shown that the metallic Ru exhibits pretty good HER activity in alkaline medium due to the higher oxophilicity of Ru[27,29] but poor OER performance. Therefore, the integration of RuO_2 and metallic Ru offers a good chance to construct an efficient bifunctional catalyst for both the OER and HER toward overall water splitting in a basic electrolyte. In fact, RuO_2 is susceptible to strong anodic corrosion and thus unable to sustain its activity during the OER process.[25] The aggregation of RuO_2 nanoparticles during the OER process is also one of the major reasons for the decline in its electrocatalytic activity. Therefore, tagging the active nanoparticles onto some supports is an efficient route to address the anodic dissolution and particle aggregation. Generally, carbon materials, such as carbon nanotubes and graphene, are attractive as excellent supports with high electrical conductivity, and are conductive to enhance the electrocatalytic activity and morphological stability of catalysts.[30–33]

Electrospinning technology is a facile method to fabricate one-dimensional (1D) elongated carbon-based materials with large aspect ratios, high electrical conductivity, tunable compositions and morphologies, and has been broadly used in a variety of electrocatalytic reactions.[34–37] Herein, based on the above concepts, we adopt a novel electrospinning–carbonization–oxidation process to construct a highly efficient bifunctional catalyst in which partially oxidized Ru nanoparticles are embedded within the 1D carbon nanofibers (RuO_2/Ru-CNFs). Owing to the configuration of the heterostructure between RuO_2 and metallic Ru as well as the favorable electrical conductivity of the CNFs, the obtained RuO_2/Ru-CNF catalyst only requires low overpotentials of 203 mV for the OER and 21 mV for the HER at 10 mA cm^{-2} in 1 M KOH. Our catalyst also shows remarkable durability in both the OER and HER processes. In addition, a home-made overall water splitting electrolyzer assembled by using RuO_2/Ru-CNFs as both the anode and cathode presents a low applied voltage of 1.452 V at 10 mA cm^{-2}, superior to the benchmark Pt/C||RuO_2 electrolyzer. In addition, the electrolyzer also presents a prominent stability for over 100 h, illustrating the potential of the RuO_2/Ru-CNFs catalyst in the field of energy storage and conversion devices.

Experimental section

Chemicals and reagents

Polyacrylonitrile (PAN, M_w = 150 000), ruthenium(III) chloride ($RuCl_3 \cdot xH_2O$), commercial ruthenium oxide (RuO_2) and Nafion solution (5 wt%) were obtained from Sigma-Aldrich. *N*,*N*-Dimethylformamide (DMF) was provided by Tianjin Tiantai Fine Chemicals Co. Ltd. Commercial Pt/C (20 wt%) was purchased from Johnson Matthey.

Preparation of RuO_2/Ru-CNFs

The RuO_2/Ru-CNF catalyst was prepared through the oxidation of Ru-CNFs by controlling the temperature during the calcination process. Firstly, a typical electrospinning technology was used to prepare the Ru precursor-PAN nanofibers. In detail, 15 mg of $RuCl_3 \cdot xH_2O$ was put into 2 g of DMF solution containing PAN (10 wt%) under constant stirring to form a homogeneous electrospinning precursor. Then a flexible Ru precursor-PAN-15 fiber membrane was obtained through an electrospinning process performed at a voltage of 16 kV and a tip-to-collector distance of 20 cm. After that, the prepared light brown Ru precursor-PAN-15 membrane was put into a tube furnace for the pyrolysis process. The membrane was pre-oxidized in air at 240 °C for 2 h, and then carbonized under an Ar atmosphere at 800 °C for 2 h to acquire the black Ru-CNFs-15 membrane. The heating rate for the entire process was fixed at 2 °C min^{-1}. Subsequently, Ru-CNFs-15 underwent an oxidative calcination process at 300, 350, 400 and 450 °C in air for 1 h, and the as-collected products were named RuO_2/Ru-CNFs-300, RuO_2/Ru-CNFs-350, RuO_2/Ru-CNFs-400 and RuO_2/Ru-CNFs-450, respectively. For comparison, the control samples were produced through a similar route with the fabrication of RuO_2/Ru-CNFs-350 but with a difference of the addition of $RuCl_3 \cdot xH_2O$ during the preparation of the electrospinning precursor, which contained 7.5 and 22.5 mg of $RuCl_3 \cdot xH_2O$ respectively. The final samples were denoted as RuO_2/Ru-CNFs-350-7.5 and RuO_2/Ru-CNFs-350-22.5.

Characterization

The morphologies of the prepared catalysts were observed by field-emission scanning electron microscopy (FESEM) (FEI Nova NanoSEM) and transmission electron microscopy (TEM) (JEOL JEM-2100). An FEI Tecnai G2 F20 electron microscope with an acceleration voltage of 200 kV was used to obtain the TEM and high-resolution TEM (HRTEM) images, selected area electron diffraction (SAED) patterns, energy dispersive X-ray (EDX) spectra and elemental mapping images of RuO_2/Ru-CNFs-350. The crystal structures of the fabricated catalysts were determined by X-ray diffraction (XRD) (PANalytical B.V. Empyrean) with Cu Kα radiation. Fourier transform infrared (FT-IR) spectra were obtained on a Thermo Scientific Nicolet iS10. X-ray photoelectron spectra (XPS) were recorded on a Thermo ESCALAB 250 spectrometer to analyze the surface oxidation states of the as-prepared samples.

Electrochemical measurements

The electrochemical measurements for the OER and HER were carried out on a CHI 760E workstation in 1 M KOH using a typical three-electrode system at ambient temperature, in which a calibrated Hg/HgO electrode (the electrode was calibrated in 1 M H_2-standard KOH through a chronoamperometry method (Fig. S1†)) and a modified rotating disk electrode (RDE, made of glassy carbon, 5 mm in diameter) were used as the reference electrode and working electrode, respectively. In addition, a Pt wire and a graphite rod were employed as the

counter electrodes for the OER and HER, respectively. To form the catalyst ink, 4 mg of catalyst was homogeneously dispersed in 1 mL of mixed solvent containing 985 μL of ethanol and 15 μL of Nafion solution with sonication. Then, 50 μL of catalyst ink was loaded onto a polished RDE and dried under infrared light, yielding a mass loading of around 1.0 mg cm^{-2}. The control sample-modified working electrodes were prepared in the same way. All the measured potentials were transformed to a reversible hydrogen electrode (RHE) according to the Nernst equation: $E_{RHE} = E_{Hg/HgO} + 0.928$ V. The linear sweep voltammetry (LSV) method was used at a sweep rate of 2 mV s^{-1} and a rotation rate of 1600 rpm. Before that, cyclic voltammetry (CV) measurements were conducted for several cycles to active and stabilize the catalyst-modified working electrode. Electrochemical impedance spectroscopy (EIS) was carried out after a quiet time for 10 s with the amplitude of the sinusoidal perturbation fixed at 5 mV. Notably, the data points of EIS for the OER were recorded at a potential of 0.54 V *vs.* Hg/HgO in a frequency range from 10 kHz to 0.01 Hz, while for the HER, the points were collected at a potential of −1.0 V *vs.* Hg/HgO in a frequency range from 10 kHz to 0.1 Hz. Unless otherwise specified, the polarization curves tested through the LSV method were corrected for 100% *iR*-compensation, following the equation $E_{corrected} = E_{measured} - iR_{\Omega}$ (R_{Ω} is the solution resistance obtained from EIS measurements). The electrochemical surface area (ECSA) values were estimated by a CV method which is illustrated in depth in the ESI.† The *i*–*t* tests for both the OER and HER were performed using the catalyst-loaded Ni foam (0.4 cm × 0.5 cm, mass loading of 3 mg cm^{-2}) as the working electrode at the required potentials. Overall water splitting was performed in 1 M KOH in a two-electrode configuration with two pieces of catalyst-loaded Ni foam (0.4 cm × 0.5 cm, mass loading of 3 mg cm^{-2}) as both the anode and cathode. The polarization curves were acquired by the LSV method at a sweep rate of 2 mV s^{-1} without *iR*-compensation. The *i*–*t* test was also conducted at a desired applied voltage.

Results and discussion

Synthesis and characterization of RuO_2/Ru-CNFs

As illustrated in Scheme 1, a facile electrospinning technique is used to produce uniform and smooth Ru precursor-PAN-15 nanofibers with an average diameter of 313 nm from FESEM measurements (Fig. S2a and b†). After a high-temperature carbonization process, the average diameter of the obtained Ru-CNFs-15 shrinks to 216 nm (Fig. S2c and d†), which is ascribed to the pyrolysis of PAN. With the subsequent calcination treatment, the surface of the nanofibers becomes obviously rough (Fig. 1a). Meanwhile, there is a significant shrinkage of the fiber diameter, especially at a higher calcination temperature, which is due to the partial loss of the carbon substrate (Fig. S3†). Moreover, the control samples with different contents of the Ru component are also investigated for their morphologies. In addition to the shrinkage of the fiber diameter

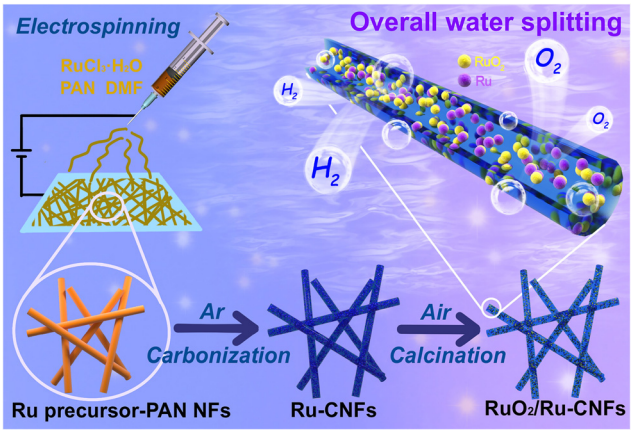

Scheme 1 Schematic diagram of the fabrication of RuO_2/Ru-CNFs.

due to original carbonization and oxidative calcination processes, the diameter of the nanofibers in each preparation process varies with different Ru contents (Fig. S4–S6†) because the addition of $RuCl_3 \cdot xH_2O$ significantly affects the viscosity of the electrospinning precursor solution, leading to a larger nanofiber diameter during the electrospinning process with the increase of the addition amount of $RuCl_3 \cdot xH_2O$. The interior morphology of the as-prepared samples is further explored using TEM images. As displayed in Fig. S7a,† plenty of small nanoparticles are embedded in Ru-CNFs-15. After the oxidative calcination process, the sizes of the nanoparticles slightly increase, but are still small (Fig. 1b and Fig. S7b–d†). With the increase of the oxidation temperature in air, the nanoparticles gradually aggregate in the case of decreased carbon preservation, accompanied by a diameter shrinkage of the nanofibers. For comparison, the influence of the proportions of the Ru component on the morphologies of the Ru-CNFs and RuO_2/Ru-CNFs has also been investigated. As shown in Fig. S8a and b,† more nanoparticles with larger sizes are observed in Ru-CNFs-22.5 with a higher Ru content. On the other hand, as the Ru-CNFs-7.5 sample with a low Ru content suffers from greater carbon losses and less presence of Ru species during the oxidation process, the obtained RuO_2/Ru-CNFs-350-7.5 possesses a smaller diameter (Fig. S8c and d†). This result demonstrates that a higher metal content in the precursor nanofibers is beneficial in maintaining the morphology of the products during the calcination treatment.

Furthermore, the HRTEM image presents well-defined crystal plane spacings of 0.318 and 0.234 nm (Fig. 1c), which correspond to the (110) plane of rutile RuO_2 and the (100) crystallographic plane of metallic Ru, demonstrating the coexistence of RuO_2 and Ru. The strong Ru signals in the EDX spectrum (Fig. 1d) confirm the presence of the Ru element in RuO_2/Ru-CNFs-350. The SAED pattern is further employed to calculate the *d*-spacings for RuO_2/Ru-CNFs-350, in which the data of the diffraction rings match well with those obtained from the following XRD results. Moreover, the high-angle annular dark-field scanning TEM (HAADF STEM) and EDX

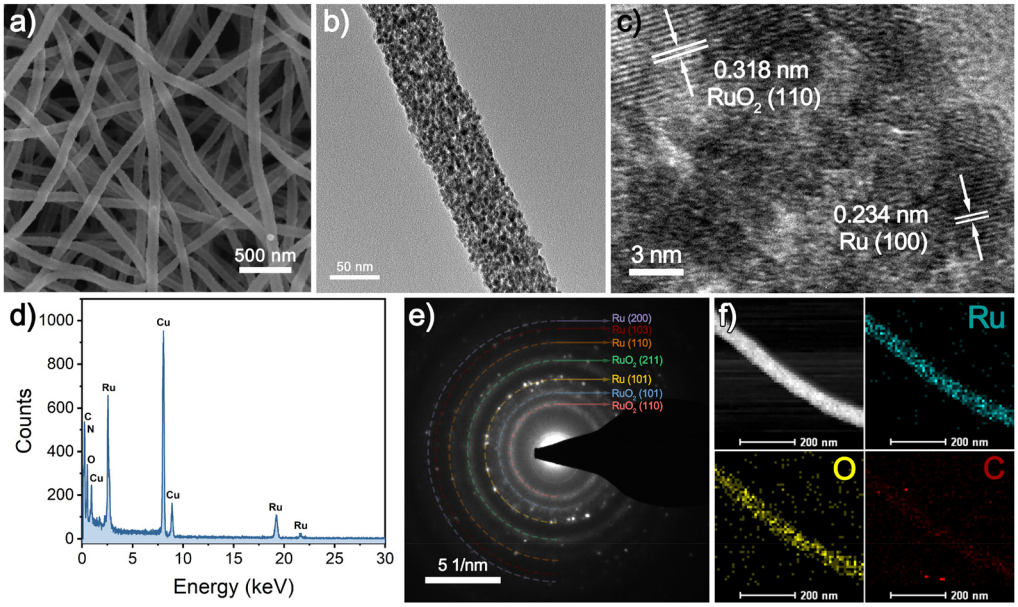

Fig. 1 (a) SEM image, (b) TEM image, (c) HRTEM image, (d) EDX spectrum, (e) SAED pattern, (f) HAADF-STEM micrograph and EDX mappings of synthesized RuO_2/Ru-CNFs-350.

mappings (Fig. 1f) show that Ru, O and C elements distribute uniformly along the nanofibers, suggesting the homogeneous distribution of Ru and RuO_2 nanoparticles in the CNFs.

The XRD patterns of the catalysts at different heating temperatures during the oxidation process are used to reveal their crystal types. As presented in Fig. 2a, after a heat-treatment in air for 1 h, there are several new diffraction peaks appearing at 28.0°, 35.1° and 54.4° at a heating temperature of 350 °C or higher, which belong to the (110), (101) and (211) planes of the rutile RuO_2 phase (JCPDS no. 43-1027), respectively. Remarkably, the characteristic peaks of RuO_2 become notably stronger with the increase of the heating temperature, demonstrating that under the condition of a heating time of 1 h, the Ru nanoparticles tend to be partially oxidized with the heating temperature over 350 °C, and this also discloses that as the temperature rises, the RuO_2 content increases. However, the remaining peaks, assigned to the Ru phase (JCPDS no. 06-0663), can be clearly observed in RuO_2/Ru-CNFs, which is stronger than that in the original Ru-CNFs-15 and RuO_2/Ru-CNFs-300. There are two possible reasons for this result: (1) as the treatment temperature increases, the crystallinity of the metallic Ru phase increases. (2) The loss of the carbon substrate causes more exposure of Ru nanoparticles, resulting in the increase of signal intensity. The XRD patterns also confirm the coexistence of the RuO_2 component and metallic Ru nanoparticles in RuO_2/Ru-CNF catalysts. Fig. S9† displays the XRD patterns of Ru-CNF and RuO_2/Ru-CNF samples with different Ru contents, revealing that the diffraction peaks corresponding to Ru and RuO_2 crystals become more obvious with the increase of the Ru content, demonstrating the formation of more nanoparticles embedded in the nanofibers. Due to the oxidation of carbon in air, FT-IR spectroscopy is used to detect the persistence of carbon in the final RuO_2/Ru-CNF products. According to the FT-IR spectrum of Ru-CNFs-15 (Fig. 2b), the peak located at 1636 cm^{-1} is associated with the C=C and C=N stretching vibrations,[38–40] and the peak at 1450 cm^{-1} is assigned to C–H bending vibrations.[40,41] The Ru-CNFs present a wide absorption peak near 1100 cm^{-1}, matching with the OH bending vibrations and C–OH stretching.[42] It can be seen that the peaks at 1636 and 1450 cm^{-1} still exist in the spectra of RuO_2/Ru-CNFs-300/350/400 samples, indicating that a part of the carbon is preserved in the oxidized samples. However, there are almost no peaks observed at a similar wavenumber in RuO_2/Ru-CNFs-450, resulting from the slight carbon preservation at a high oxidation temperature. Additionally, the peak appearing at 1250 cm^{-1} in the FT-IR spectra of RuO_2/Ru-CNFs corresponds to the in-plane bending vibrations or C–N vibrations.[39,40] Because of the oxidation treatment, the peaks detected at 1200–1000 cm^{-1} may correspond to C–O vibrations.[40,41,43]

XPS measurements are further employed to reveal the surface composition and oxidation states of Ru-CNFs-15 and RuO_2/Ru-CNFs-350. The full surveys of the catalysts confirm the appearance of Ru, O and C elements (Fig. S10a and b†). As illustrated in the narrow-scan XPS spectrum of Ru 3p of Ru-CNFs-15 (Fig. 2c), the spin–orbit peaks at 484.2 and 462.3 eV correspond to Ru^0 $3p_{1/2}$ and Ru^0 $3p_{3/2}$, respectively.[27] For RuO_2/Ru-CNFs-350, the appearance of Ru^{4+} $3p_{1/2}$ and Ru^{4+} $3p_{3/2}$ in the RuO_2 phase located at 486.6 and 464.2 eV demonstrates the partial oxidation of catalysts after the heating process.[18,44] Furthermore, Fig. 2d shows that the deconvolution of the O 1s spectrum of Ru-CNFs-15 provides three major peaks at binding energies of 533.4 (O4), 532.0 (O3) and

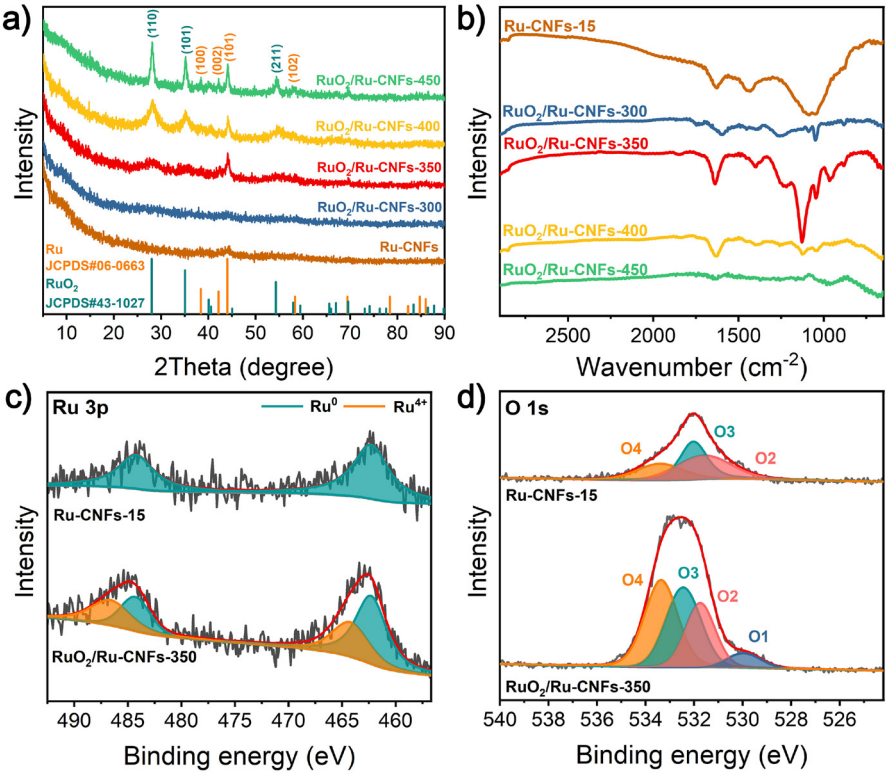

Fig. 2 (a) XRD patterns and (b) FT-IR spectra of Ru-CNFs-15 and different RuO_2/Ru-CNF catalysts. Narrow-scan XPS spectra of (c) Ru 3p and (d) O 1s of Ru-CNFs-15 and RuO_2/Ru-CNFs-350.

531.6 eV (O2) corresponding to the C–O bond, the surface molecular water and the surface hydroxyl group, respectively.[31,45] In particular, there is a characteristic peak appearing at 530.0 eV (O1) indexed to the lattice oxygen (Ru–O) in the O 1s spectrum of RuO_2/Ru-CNFs-350, further verifying the formation of RuO_2 on the catalyst.[46,47] The peaks centered at 284.1 and 280.6 eV in the narrow-scan Ru 3d spectrum of Ru-CNFs-15 (Fig. S10c†) can be resolved to Ru $3d_{3/2}$ and Ru $3d_{5/2}$, respectively.[45,48,49] For RuO_2/Ru-CNFs-350 presented in Fig. S10d,† the binding energy peaks of Ru 3d are observed at 284.5 and 280.9 eV, which exhibit positive shifts compared to those of Ru-CNFs-15, thus demonstrating the change of the electronic structure of Ru due to the construction of the RuO_2/Ru heterostructure. The C 1s spectrum, which is partially overlapped with Ru $3d_{3/2}$, is deconvoluted into three binding energy peaks at 287.6, 285.5 and 284.6 eV, which are ascribed to C═O, C–O and C–C/C═C, respectively.[27,44]

Oxygen evolution activity

The OER property is measured by coating the catalyst on the RDE and then assembling a typical three-electrode configuration in 1 M KOH. After the 100% *iR* drop compensation, the RuO_2/Ru-CNFs-350 catalyst exhibits the best OER activity with an overpotential of 203 mV at 10 mA cm^{-2} (Fig. 3a), which is the lowest value among all the catalysts including RuO_2/Ru-CNFs-300 (over 470 mV), RuO_2/Ru-CNFs-400 (212 mV), RuO_2/Ru-CNFs-450 (256 mV), Ru-CNFs-15 (over 470 mV), and commercial RuO_2 (339 mV). Moreover, at the current densities of 100 and 200 mA cm^{-2}, the RuO_2/Ru-CNFs-350 catalyst possesses ultralow potentials of 256 and 280 mV, respectively, outperforming many other reported noble metal-based catalysts (Table S1†). Furthermore, the RuO_2/Ru-CNFs-350 catalysts display far better performance than the Ru-CNFs-15 sample, indicating that the heterostructure constructed with Ru and RuO_2 is beneficial for boosting the OER activity and the optimized heating temperature during the oxidation process is 350 °C. In addition, the RuO_2/Ru-CNF catalysts calcined at temperatures of 350 °C and 400 °C exhibit much better electrocatalytic activity than those heated at 450 °C. This is because the calcination temperature can regulate the oxidation state of metallic Ru and further affect the construction of RuO_2/Ru heterostructures, which provide main active sites during the electrochemical process.[6] Moreover, the preserved-carbon matrix can not only avoid the aggregation of active nanoparticles to expose more active sites but also improve the charge transfer of catalysts, which benefits the promotion of the electrocatalytic performances.[37] Tafel slopes, a vital parameter to evaluate the reaction mechanism of the catalysts,[50] are calculated according to the following Tafel equation: $\eta = b\log|j| + a$, where b is the Tafel slope value. As shown in Fig. 3b, RuO_2/Ru-CNFs-350 presents the lowest Tafel slope of 40.0 mV dec^{-1} compared with RuO_2/Ru-CNFs-300 (188.2 mV dec^{-1}), RuO_2/Ru-CNFs-400 (46.3 mV dec^{-1}), RuO_2/Ru-CNFs-450 (52.9 mV dec^{-1}) and commercial RuO_2 (91.5 mV dec^{-1}). In

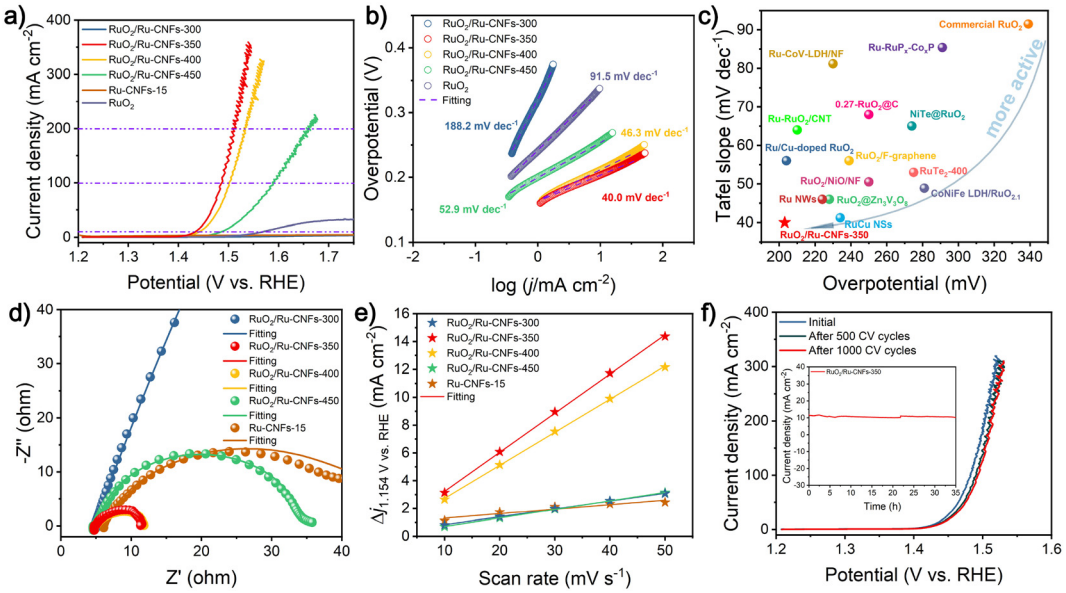

Fig. 3 OER measurements in 1 M KOH. (a) Polarization curves and (b) Tafel plots of different catalysts. (c) Comparison of some representative catalysts for OER properties. (d) Nyquist plots of different catalysts at a potential of 0.54 V *vs.* Hg/HgO in an enlarged region in Fig. S12.† The dots and lines represent the experimental and fitting data, respectively. (e) Capacitive current density of different catalysts with linear fitting with different scan rates at 1.154 V *vs.* RHE. (f) Polarization curves before and after 500 and 1000 CV cycles and (f, inset) the *i*–*t* curve of RuO_2/Ru-CNFs-350 at 1.448 V *vs.* RHE.

general, a smaller Tafel slope means that the rate-determining step (RDS) is closer to the end of the multi-electron transfer reaction.[51–53] The Tafel slope of 40 mV dec^{-1} suggests that the RDS is the chemisorption and dissociation of OH^- ($M - OH + OH^- \rightarrow M - O + H_2O + e^-$, where M is the active site of the catalyst).[54–56] Subsequently, the overall performances of our RuO_2/Ru-CNFs-350 catalyst and some recently reported Ru-based catalysts are visualized in Fig. 3c (the details are listed in Table S1†), revealing that RuO_2/Ru-CNFs-350 exhibits outstanding electrocatalytic activity toward the OER, superior to many other mentioned catalysts. Furthermore, Fig. S11† presents the OER performances of RuO_2/Ru-CNFs-350 catalysts obtained by adding different Ru contents during the electrospinning procedure, and the RuO_2/Ru-CNFs-350-15 catalyst apparently shows the best OER activity.

EIS measurements are further performed to study the charge transfer resistance (R_{ct}) of the obtained electrocatalysts for the OER, and it is generally reflected by the semicircle in the low frequency range from the Nyquist plots. As illustrated in Fig. 3d and Fig. S12,† after the obtained experimental points are fitted by a typical equivalent circuit (Fig. S13†), the R_{ct} of as-prepared RuO_2/Ru-CNFs-350 is determined to be 6.37 Ω, which is the lowest value among all the measured samples (Table S2†). The smaller R_{ct} value means faster charge transfer capacity and outstanding reaction kinetics.[57] In particular, the RuO_2/Ru-CNFs-300 catalyst exhibits a large charge transfer resistance for the OER process, indicating its sluggish OER kinetics, and almost no activity of the OER over the entire applied potential range also corresponds to this result (Fig. 3a). From the afore-mentioned morphology and chemical composition analyses, it can be inferred that the construction of the RuO_2/Ru heterostructure and the excellent electrical conductivity of carbon matrix are beneficial for the electron transfer to improve the OER performance.[6] Furthermore, the electrocatalytic activity of our fabricated catalysts is assessed *via* the ECSA value estimated from the double layer capacitance (C_{dl}), which is evaluated by a simple CV method (Fig. S14a–e†). Based on the plots of capacitive current density *versus* scan rates (Fig. 3e), the C_{dl} of the RuO_2/Ru-CNFs-350 catalyst is found to have the largest value of 140.6 mF cm^{-2} compared with RuO_2/Ru-CNFs-300 (28.3 mF cm^{-2}), RuO_2/Ru-CNFs-400 (118.9 mF cm^{-2}), RuO_2/Ru-CNFs-450 (30.7 mF cm^{-2}) and Ru-CNFs-15 (16.2 mF cm^{-2}) (Fig. S14f†). Therefore, the ECSA and roughness factor (RF) values are estimated and exhibited in Table S3,† where the RuO_2/Ru-CNFs-350 catalyst still displays the largest values, significantly exceeding those of other control samples. A higher ECSA suggests larger surface roughness and more exposed active sites, generally resulting in better electrocatalytic performance.[58,59]

Durability is critical for catalysts to assess the OER performance in practical applications. Fig. 3f presents the polarization curves of RuO_2/Ru-CNFs-350 before and after 500 and 1000 CV cycles. Apparently, the current density only slightly decreases after 500 CV cycles and then hardly changes until 1000 CV cycles, verifying the excellent cycling stability of RuO_2/Ru-CNFs-350. The *i*–*t* curve of RuO_2/Ru-CNFs-350 also illustrates the outstanding long-term durability for 35 h at 1.448 V *vs.* RHE (inset plots in Fig. 3f). Generally speaking, the nanoparticles tend to aggregate during electrochemical processes, causing a decline in electrocatalytic activity.[60] However, the

RuO_2/Ru-CNFs-350 catalysts exhibit prominent electrocatalytic stability, which implies that the carbon matrix in our synthesized catalyst may restrict the aggregation of active nanoparticles. To investigate the changes of the RuO_2/Ru-CNFs-350 catalyst during the OER process, the catalyst after *i–t* measurements is collected and subjected to a series of characterization processes. The SEM image (Fig. S15a†) reveals the well-preserved nanofibrous morphology of the RuO_2/Ru-CNFs-350 catalyst, confirming its structural robustness, and the diffraction peaks of Ru and RuO_2 crystals are consistent with the initial ones from the XRD pattern (Fig. S15b†), further demonstrating the structural stability of the RuO_2/Ru-CNFs-350 catalyst. Since the OER process usually occurs at the catalyst surface, XPS analysis is carried out to study the oxidation state changes on the surface of the catalyst after the OER procedure. As illustrated in Fig. S15c,† the Ru 3p state of RuO_2/Ru-CNFs-350 after the long-term OER test exhibits similar features to those before the test while the ratio of Ru^0/Ru^{4+} slightly decreases, indicating the oxidation of partial metallic Ru in the RuO_2/Ru-CNFs-350 catalyst because of the anodic potentials.[44] Moreover, the increase of the percentage of O1 species (lattice oxygen contribution) observed in the O 1s spectra (Fig. S15d†) further confirms the oxidation during the OER process.

Hydrogen evolution activity

The electrocatalytic performances of the concerned catalysts toward the HER in 1 M KOH are further investigated, aiming to use them as high-efficiency bifunctional catalysts for overall water splitting. As illustrated in Fig. 4a and b, the RuO_2/Ru-CNFs-350 catalyst only requires an overpotential of 21 mV to deliver a current density of 10 mA cm^{-2} after the 100% *iR* drop compensation, lower than those of RuO_2/Ru-CNFs-300 (41 mV), RuO_2/Ru-CNFs-400 (40 mV), RuO_2/Ru-CNFs-450 (45 mV) and Ru-CNFs-15 (23 mV) catalysts, and greatly outperforms many other similar reported electrocatalysts (Table S4†). This result demonstrates the promising prospects of our partially oxidized Ru-based catalysts for HER applications in alkaline electrolytes. It is worth mentioning that the RuO_2/Ru-CNFs-350 catalyst displays the best HER overpotential of only 99 mV at a high current density of 150 mA cm^{-2}, surpassing those of the prepared control catalysts by a great margin, which is probably ascribed to the construction of the distinct RuO_2/Ru heterostructure and the favorable electrical conductivity of the preserved carbon matrix. Additionally, the required overpotential of the RuO_2/Ru-CNFs-350 catalyst is slightly lower than that of commercial Pt/C at certain current densities in the applied potential range, indicating that the synthesized RuO_2/Ru-CNFs-350 catalyst exhibits comparable electrocatalytic activity to the best commercial HER catalyst. To study the mechanism of the HER process, the following Tafel analysis is performed. Fig. 4c reveals that the RuO_2/Ru-CNFs-350 catalyst displays a Tafel slope of 25.1 mV dec^{-1}, which is less than those of other prepared catalysts and similar to that of Pt/C. In particular, the Tafel slope value decreases from 46.5 mV dec^{-1} for Ru-CNFs-15 to 25.1 mV dec^{-1} for RuO_2/Ru-CNFs-350 after the oxidation process, which suggests that the mechanism of the HER process changes from the Volmer–Heyrovsky mechanism to the Volmer–Tafel mechanism, leading to a significant improvement of HER performance. The Tafel step ($M - H_{ads} + M - H_{ads} \rightarrow H_2 + 2M$, where M is the active site of the catalyst) is the RDS in this case.[61–63] Among the RuO_2/Ru-

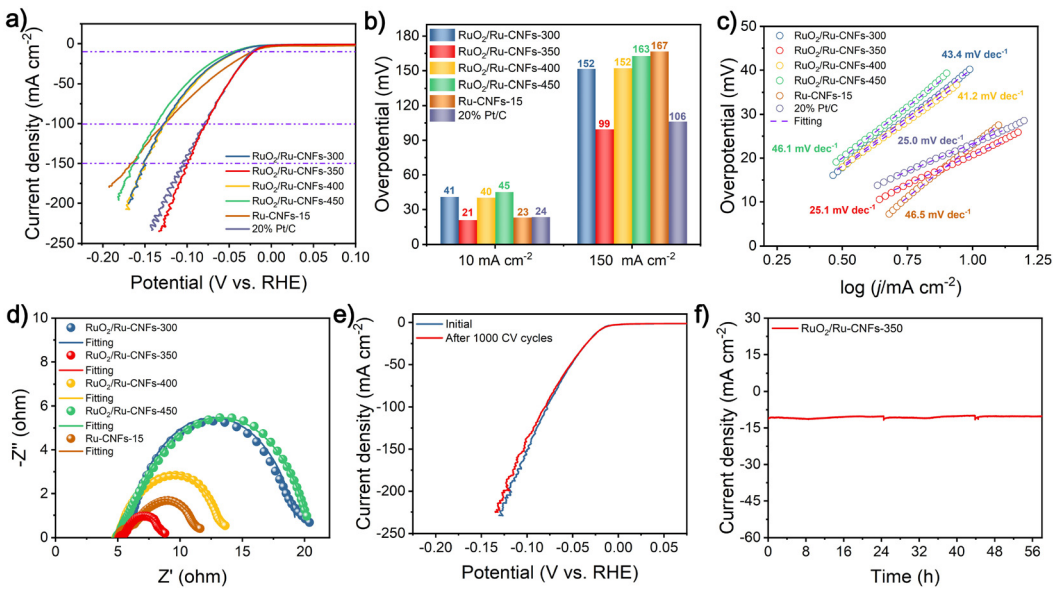

Fig. 4 HER measurements in 1 M KOH. (a) Polarization curves of different catalysts. (b) Comparison of the overpotentials of different catalysts at 10 and 150 mA cm^{-2}. (c) Tafel plots of different catalysts. (d) Nyquist plots of different catalysts at a potential of −1 V *vs.* Hg/HgO. The dots and lines represent the experimental and fitting data, respectively. (e) Polarization curves before and after 1000 CV cycles and (f) the *i–t* curve of the RuO_2/Ru-CNFs-350 catalyst at −0.027 V *vs.* RHE.

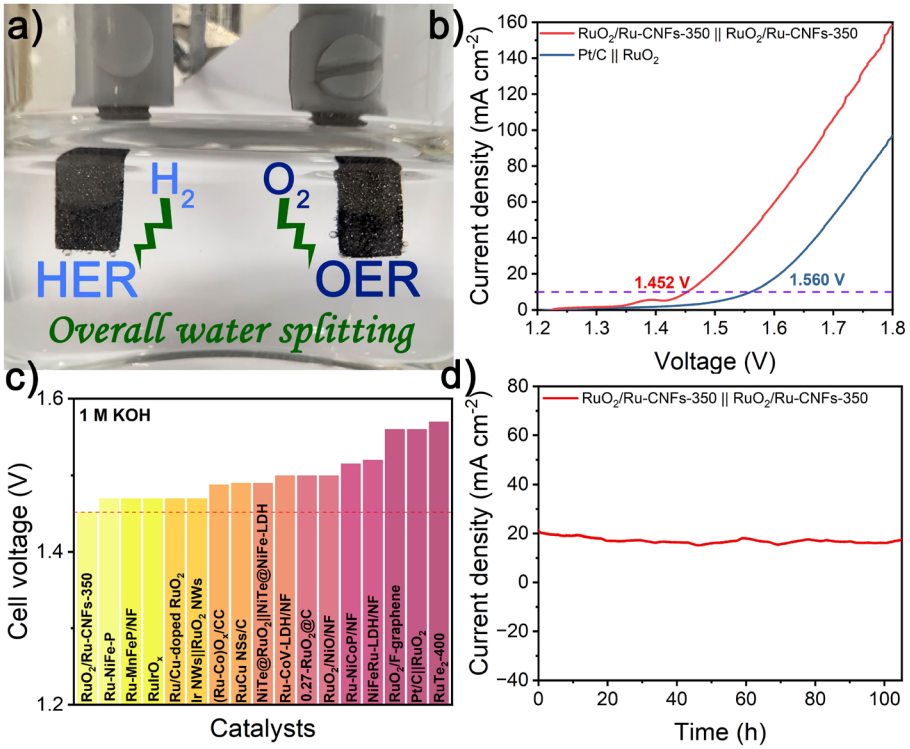

Fig. 5 Overall water splitting measurements in 1 M KOH. (a) Digital graph of the RuO_2/Ru-CNFs-350||RuO_2/Ru-CNFs-350 electrolyzer. (b) Polarization curves of the RuO_2/Ru-CNFs-350||RuO_2/Ru-CNFs-350 and the benchmark Pt/C||RuO_2 electrolyzers. (c) Cell voltage of the RuO_2/Ru-CNFs-350||RuO_2/Ru-CNFs-350 electrolyzer at 10 mA cm^{-2} in contrast to the reported electrolyzers. (d) The *i*–*t* curves of RuO_2/Ru-CNFs-350||RuO_2/Ru-CNFs-350 at a voltage of 1.47 V.

CNFs-350 catalysts with different Ru contents, the RuO_2/Ru-CNFs-350-15 catalyst exhibits the best performance for the HER (Fig. S16†).

Furthermore, the R_{ct} of the RuO_2/Ru-CNFs-350 catalyst is acquired from the fitted Nyquist plot, which is the smallest value of 3.26 Ω among all the control catalysts (Fig. 4d and Table S5†). This result also discloses its prominent kinetics and excellent activity for the HER. Fig. 4e displays the satisfactory cycling stability of RuO_2/Ru-CNFs-350 for the HER with little decrease in current density after 1000 CV cycles. Moreover, the RuO_2/Ru-CNFs-350 catalyst also presents a remarkable long-term stability for 58 h with a slight decline during the *i*–*t* measurements for the HER (Fig. 4f). The morphology and chemical structure of the RuO_2/Ru-CNFs-350 catalyst after the HER process are characterized as follows. First of all, the SEM image shows that the fibrous structure of RuO_2/Ru-CNFs-350 is well maintained after the long-term measurement, suggesting the structural stability for the HER (Fig. S17a†). In addition, the diffraction peaks of Ru and RuO_2 crystals are still well preserved and are clearly observed from the XRD pattern (Fig. S17b†). Finally, from the XPS spectra of Ru 3p and O 1s before and after the *i*–*t* test of the HER (Fig. S17c and d†), there is no significant change in the positions of the characteristic peaks, demonstrating the prominent stability of our RuO_2/Ru-CNFs-350 catalyst during the HER process.

Overall water splitting

The overall water splitting measurements are conducted in 1 M KOH on a two-electrode configuration equipped with Ni foam-supported RuO_2/Ru-CNFs-350 as both the cathode and anode. A lot of bubbles are generated from electrodes during the overall water splitting process, which can be clearly observed from the digital graph and video of the RuO_2/Ru-CNFs-350||RuO_2/Ru-CNFs-350 electrolyzer (Fig. 5a and ESI Video†). Fig. 5b illustrates that the RuO_2/Ru-CNFs-350||RuO_2/Ru-CNFs-350 device requires a low cell voltage of 1.452 V to achieve 10 mA cm^{-2}, about 110 mV less than that of the benchmark Pt/C||RuO_2 system, outperforming many other reported Ru-based electrolyzers (Fig. 5c and Table S6†). Moreover, the RuO_2/Ru-CNFs-350||RuO_2/Ru-CNFs-350 electrolyzer exhibits prominent durability in the continuous *i*–*t* measurement for over 100 h (Fig. 5d). It confirms that our water-splitting device can extremely reduce the energy consumption, proving its broad prospects for practical application in the water decomposition field.

Conclusions

In summary, the 1D elongated RuO_2/Ru-CNFs-350 catalyst is prepared *via* an electrospinning–carbonization procedure and the oxidation process of the obtained Ru-CNFs as a bifunc-

tional electrocatalyst toward overall water splitting. Our investigation reveals that the formation of the heterostructure between RuO_2 and metallic Ru provides more catalytically active sites, which are beneficial for enhanced OER and HER performances. In addition, the preserved carbon matrix in the RuO_2/Ru-CNFs-350 catalyst not only promotes the electrical conductivity but also restrains nanoparticle aggregation during the electrocatalytic reactions, endowing it with a remarkable durability toward both the OER and HER. Particularly, the overall water splitting electrolyzer constructed with RuO_2/Ru-CNFs-350 as the electrode presents a much better electrocatalytic performance than the benchmark Pt/C||RuO_2 system. This work affords new inspiration to fabricate more efficient electrocatalysts for advanced energy-related applications.

Author contributions

Xiaofeng Lu and Ce Wang proposed the idea and supervised the program. Mengxiao Zhong performed the experiments and analyzed the data. Su Yan and Jiaqi Xu participated in the data analysis and discussions. Mengxiao Zhong wrote the manuscript and Xiaofeng Lu revised it.

Conflicts of interest

The authors declare that they have no conflict of interest.

Acknowledgements

This work was financially supported by the National Natural Science Foundation of China (51973079 and 21875084) and the Project of the Education Department of Jilin Province, China (JJKH20211047KJ).

Notes and references

1 Y. Bu, S. Joo, Y. Zhang, Y. Wang, D. Meng, X. Ge and G. Kim, A highly efficient composite cathode for proton-conducting solid oxide fuel cells, *J. Power Sources*, 2020, **451**, 227812.

2 C. Z. Yuan, Z. T. Sun, Y. F. Jiang, Z. K. Yang, N. Jiang, Z. W. Zhao, U. Y. Qazi, W. H. Zhang and A. W. Xu, One-step in situ growth of iron-nickel sulfide nanosheets on FeNi alloy foils: High-performance and self-supported electrodes for water oxidation, *Small*, 2017, **13**, 1604161.

3 W. Zhu, T. Zhang, Y. Zhang, Z. Yue, Y. Li, R. Wang, Y. Ji, X. Sun and J. Wang, A practical-oriented NiFe-based water-oxidation catalyst enabled by ambient redox and hydrolysis co-precipitation strategy, *Appl. Catal., B*, 2019, **244**, 844–852.

4 T. Y. Ma, J. L. Cao, M. Jaroniec and S. Z. Qiao, Interacting carbon nitride and titanium carbide nanosheets for high-performance oxygen evolution, *Angew. Chem., Int. Ed.*, 2016, **55**, 1138–1142.

5 J. Cai, J. Ding, D. Wei, X. Xie, B. Li, S. Lu, J. Zhang, Y. Liu, Q. Cai and S. Zang, Coupling of Ru and O–vacancy on 2D Mo–based electrocatalyst via a solid–phase interface reaction strategy for hydrogen evolution reaction, *Adv. Energy Mater.*, 2021, **11**, 2100141.

6 R. Jiang, D. T. Tran, J. Li and D. Chu, Ru@RuO_2 core–shell nanorods: A highly active and stable bifunctional catalyst for oxygen evolution and hydrogen evolution reactions, *Energy Environ. Mater.*, 2019, **2**, 201–208.

7 C. Wei, R. R. Rao, J. Peng, B. Huang, I. E. L. Stephens, M. Risch, Z. J. Xu and Y. Shao-Horn, Recommended practices and benchmark activity for hydrogen and oxygen electrocatalysis in water splitting and fuel cells, *Adv. Mater.*, 2019, **31**, 1806296.

8 X. Zou and Y. Zhang, Noble metal-free hydrogen evolution catalysts for water splitting, *Chem. Soc. Rev.*, 2015, **44**, 5148–5180.

9 Q. Gao, W. Zhang, Z. Shi, L. Yang and Y. Tang, Structural design and electronic modulation of transition-metal-carbide electrocatalysts toward efficient hydrogen evolution, *Adv. Mater.*, 2019, **31**, 1802880.

10 J. Yao, W. Huang, W. Fang, M. Kuang, N. Jia, H. Ren, D. Liu, C. Lv, C. Liu, J. Xu and Q. Yan, Promoting electrocatalytic hydrogen evolution reaction and oxygen evolution reaction by fields: Effects of electric field, magnetic field, strain, and light, *Small Methods*, 2020, **4**, 2000494.

11 Y. Ding, B.-Q. Miao, S.-N. Li, Y.-C. Jiang, Y.-Y. Liu, H.-C. Yao and Y. Chen, Benzylamine oxidation boosted electrochemical water-splitting: Hydrogen and benzonitrile co-production at ultra-thin Ni_2P nanomeshes grown on nickel foam, *Appl. Catal., B*, 2020, **268**, 118393.

12 S. Gupta, N. Patel, R. Fernandes, R. Kadrekar, A. Dashora, A. K. Yadav, D. Bhattacharyya, S. N. Jha, A. Miotello and D. C. Kothari, Co–Ni–B nanocatalyst for efficient hydrogen evolution reaction in wide pH range, *Appl. Catal., B*, 2016, **192**, 126–133.

13 Y. Zhao, S. Xing, X. Meng, J. Zeng, S. Yin, X. Li and Y. Chen, Ultrathin Rh nanosheets as a highly efficient bifunctional electrocatalyst for isopropanol-assisted overall water splitting, *Nanoscale*, 2019, **11**, 9319–9326.

14 X. Cui, P. Ren, C. Ma, J. Zhao, R. Chen, S. Chen, N. P. Rajan, H. Li, L. Yu, Z. Tian and D. Deng, Robust interface Ru centers for high-performance acidic oxygen evolution, *Adv. Mater.*, 2020, **32**, 1908126.

15 W. Li, S. Chen, M. Zhong, C. Wang and X. Lu, Synergistic coupling of NiFe layered double hydroxides with Co-C nanofibers for high-efficiency oxygen evolution reaction, *Chem. Eng. J.*, 2021, **415**, 128879.

16 X. Li, X. Hao, A. Abudula and G. Guan, Nanostructured catalysts for electrochemical water splitting: current state and prospects, *J. Mater. Chem. A*, 2016, **4**, 11973–12000.

17 Z. Liu, X. Yu, H. Xue and L. Feng, A nitrogen-doped CoP nanoarray over 3D porous Co foam as an efficient bifunc-

tional electrocatalyst for overall water splitting, *J. Mater. Chem. A*, 2019, **7**, 13242–13248.
18 K. Yang, P. Xu, Z. Lin, Y. Yang, P. Jiang, C. Wang, S. Liu, S. Gong, L. Hu and Q. Chen, Ultrasmall Ru/Cu-doped RuO_2 complex embedded in amorphous carbon skeleton as highly active bifunctional electrocatalysts for overall water splitting, *Small*, 2018, **14**, 1803009.
19 Y. Bu, G. Nam, S. Kim, K. Choi, Q. Zhong, J. Lee, Y. Qin, J. Cho and G. Kim, A tailored bifunctional electrocatalyst: boosting oxygen reduction/evolution catalysis via electron transfer between N-doped graphene and perovskite oxides, *Small*, 2018, **14**, 1802767.
20 J. Yang, Y. Ji, Q. Shao, N. Zhang, Y. Li and X. Huang, A universal strategy to metal wavy nanowires for efficient electrochemical water splitting at pH-universal conditions, *Adv. Funct. Mater.*, 2018, **28**, 1803722.
21 W. Song, M. Li, C. Wang and X. Lu, Electronic modulation and interface engineering of electrospun nanomaterials–based electrocatalysts toward water splitting, *Carbon Energy*, 2020, **3**, 101–128.
22 Y. Lee, J. Suntivich, K. J. May, E. E. Perry and Y. Shao-Horn, Synthesis and activities of rutile IrO_2 and RuO_2 nanoparticles for oxygen evolution in acid and alkaline solutions, *J. Phys. Chem. Lett.*, 2012, **3**, 399–404.
23 D. L. Burnett, E. Petrucco, K. M. Rigg, C. M. Zalitis, J. G. Lok, R. J. Kashtiban, M. R. Lees, J. D. B. Sharman and R. I. Walton, $(M,Ru)O_2$ (M = Mg, Zn, Cu, Ni, Co) rutiles and their use as oxygen evolution electrocatalysts in membrane electrode assemblies under acidic conditions, *Chem. Mater.*, 2020, **32**, 6150–6160.
24 K. A. Stoerzinger, R. R. Rao, X. R. Wang, W. T. Hong, C. M. Rouleau and Y. Shao-Horn, The role of Ru redox in pH-dependent oxygen evolution on rutile ruthenium dioxide surfaces, *Chem*, 2017, **2**, 668–675.
25 A. Yu, M. H. Kim, C. Lee and Y. Lee, Structural transformation between rutile and spinel crystal lattices in Ru-Co binary oxide nanotubes: enhanced electron transfer kinetics for the oxygen evolution reaction, *Nanoscale*, 2021, **13**, 13776–13785.
26 Z. Liu, M. Zha, Q. Wang, G. Hu and L. Feng, Overall water-splitting reaction efficiently catalyzed by a novel bi-functional Ru/Ni_3N-Ni electrode, *Chem. Commun.*, 2020, **56**, 2352–2355.
27 M. Li, H. Wang, W. Zhu, W. Li, C. Wang and X. Lu, RuNi nanoparticles embedded in N-doped carbon nanofibers as a robust bifunctional catalyst for efficient overall water splitting, *Adv. Sci.*, 2020, **7**, 1901833.
28 X. Yang, Z. Zhao, X. Yu and L. Feng, Electrochemical hydrogen evolution reaction boosted by constructing Ru nanoparticles assembled as a shell over semimetal Te nanorod surfaces in acid electrolyte, *Chem. Commun.*, 2019, **55**, 1490–1493.
29 W. Li, B. Feng, L. Yi, J. Li and W. Hu, Highly efficient alkaline water splitting with Ru-doped Co-V layered double hydroxide nanosheets as a bifunctional electrocatalyst, *ChemSusChem*, 2021, **14**, 730–737.
30 W. Li, C. Wang and X. Lu, Integrated transition metal and compounds with carbon nanomaterials for electrochemical water splitting, *J. Mater. Chem. A*, 2021, **9**, 3786–3827.
31 Y. Li, Y. Wang, J. Lu, B. Yang, X. San and Z.-S. Wu, 2D intrinsically defective RuO_2/graphene heterostructures as all-pH efficient oxygen evolving electrocatalysts with unprecedented activity, *Nano Energy*, 2020, **78**, 105185.
32 Z. Zhu, Y. Ni, Q. Lv, J. Geng, W. Xie, F. Li and J. Chen, Surface plasmon mediates the visible light–responsive lithium–oxygen battery with Au nanoparticles on defective carbon nitride, *Proc. Natl. Acad. Sci. U. S. A.*, 2021, **118**, e2024619118.
33 H. Yang, Y. Liu, X. Liu, X. Wang, H. Tian, G. I. N. Waterhouse, P. E. Kruger, S. G. Telfer and S. Ma, Large-scale synthesis of N-doped carbon capsules supporting atomically dispersed iron for efficient oxygen reduction reaction electrocatalysis, *eScience*, 2022, **2**, 227–234.
34 N. Song, S. Ren, Y. Zhang, C. Wang and X. Lu, Confinement of Prussian blue analogues inside conducting polymer nanotubes enables significantly enhanced catalytic performance for water treatment, *Adv. Funct. Mater.*, 2022, **32**, 2204751.
35 N. Song, M. Zhong, J. Xu, C. Wang and X. Lu, Single-atom iron confined within polypyrrole-derived carbon nanotubes with exceptional peroxidase-like activity for total antioxidant capacity, *Sens. Actuators, B*, 2022, **351**, 130969.
36 M. Zhong, W. Li, C. Wang and X. Lu, Synthesis of hierarchical nickel sulfide nanotubes for highly efficient electrocatalytic urea oxidation, *Appl. Surf. Sci.*, 2022, **575**, 151708.
37 M. Zhong, N. Song, C. Li, C. Wang, W. Chen and X. Lu, Controllable growth of Fe-doped NiS_2 on NiFe-carbon nanofibers for boosting oxygen evolution reaction, *J. Colloid Interface Sci.*, 2022, **614**, 556–565.
38 X. Yan, Z. Tai, J. Chen and Q. Xue, Fabrication of carbon nanofiber-polyaniline composite flexible paper for supercapacitor, *Nanoscale*, 2011, **3**, 212–216.
39 S. Radu, J. Silviu, S. Tanta, K. Wilhelm, K. Shodo and O. Zenjiro, IR and X-ray characterization of the ferromagnetic phase of pyrolysed polyacrylonitrile, *Carbon*, 1999, **37**, 1–6.
40 V. Tucureanu, A. Matei and A. M. Avram, FTIR Spectroscopy for Carbon Family Study, *Crit. Rev. Anal. Chem.*, 2016, **46**, 502–520.
41 L.-h. Teng and T.-d. Tang, IR study on surface chemical properties of catalytic grown carbon nanotubes and nanofibers, *J. Zhejiang Univ., Sci., A*, 2008, **9**, 720–726.
42 X. Li, X. Xiang, Y. Liu and D. Xiao, Template-free fabrication of hollow N-doped carbon sphere (h-NCS) to synthesize h-NCS@PANI positive material for MoO3// h-NCS@PANI asymmetric supercapacitor, *Appl. Surf. Sci.*, 2018, **442**, 476–486.
43 Y. G. Wang, H. Q. Li and Y. Y. Xia, Ordered whiskerlike polyaniline grown on the surface of mesoporous carbon and its electrochemical capacitance performance, *Adv. Mater.*, 2006, **18**, 2619–2623.

44 B. Tang, X. Yang, Z. Kang and L. Feng, Crystallized $RuTe_2$ as unexpected bifunctional catalyst for overall water splitting, *Appl. Catal., B*, 2020, **278**, 119281.

45 S. Niu, X.-P. Kong, S. Li, Y. Zhang, J. Wu, W. Zhao and P. Xu, Low Ru loading $RuO_2/(Co,Mn)_3O_4$ nanocomposite with modulated electronic structure for efficient oxygen evolution reaction in acid, *Appl. Catal., B*, 2021, **297**, 120442.

46 Y. Jiang, Z. Geng, L. Yuan, Y. Sun, Y. Cong, K. Huang, L. Wang and W. Zhang, Nanoscale architecture of $RuO_2/La_{0.9}Fe_{0.92}Ru_{0.08-x}O_{3-\delta}$ composite via manipulating the exsolution of low Ru-substituted A-site deficient perovskite, *ACS Sustainable Chem. Eng.*, 2018, **6**, 11999–12005.

47 M. Li, Y. Zhu, H. Wang, C. Wang, N. Pinna and X. Lu, Ni strongly coupled with Mo_2C encapsulated in nitrogen-doped carbon nanofibers as robust bifunctional catalyst for overall water splitting, *Adv. Energy Mater.*, 2019, **9**, 1803185.

48 Z. Peng, H. Wang, L. Zhou, Y. Wang, J. Gao, G. Liu, S. A. T. Redfern, X. Feng, S. Lu, B. Li and Z. Liu, Hollow carbon shells enhanced by confined ruthenium as cost-efficient and superior catalysts for the alkaline hydrogen evolution reaction, *J. Mater. Chem. A*, 2019, **7**, 6676–6685.

49 W. Wang, H. Liu, T. Wu, P. Zhang, G. Ding, S. Liang, T. Jiang and B. Han, Ru catalyst supported on bentonite for partial hydrogenation of benzene to cyclohexene, *J. Mol. Catal. A: Chem.*, 2012, **355**, 174–179.

50 M. Chatenet, J. Benziger, M. Inaba, S. Kjelstrup, T. Zawodzinski and R. Raccichini, Good practice guide for papers on fuel cells and electrolysis cells for the Journal of Power Sources, *J. Power Sources*, 2020, **451**, 227635.

51 S. Anantharaj and V. Aravindan, Developments and perspectives in 3d transition–metal–based electrocatalysts for neutral and near–neutral water electrolysis, *Adv. Energy Mater.*, 2019, **10**, 1902666.

52 K. N. Dinh, Y. Sun, Z. Pei, Z. Yuan, A. Suwardi, Q. Huang, X. Liao, Z. Wang, Y. Chen and Q. Yan, Electronic modulation of nickel disulfide toward efficient water electrolysis, *Small*, 2020, **16**, 1905885.

53 T. Shinagawa, A. T. Garcia-Esparza and K. Takanabe, Insight on Tafel slopes from a microkinetic analysis of aqueous electrocatalysis for energy conversion, *Sci. Rep.*, 2015, **5**, 13801.

54 X. Wang, L. Li, Z. Wang, L. Tan, Z. Wu, Z. Liu, S. Gai and P. Yang, NiS_2/MoS_2 on carbon cloth as a bifunctional electrocatalyst for overall water splitting, *Electrochim. Acta*, 2019, **326**, 134983.

55 R. Djara, M. A. Lacour, A. Merzouki, J. Cambedouzou, D. Cornu, S. Tingry and Y. Holade, Iridium and ruthenium modified polyaniline polymer leads to nanostructured electrocatalysts with high performance regarding water splitting, *Polymers*, 2021, **13**, 190.

56 T. Audichon, T. W. Napporn, C. Canaff, C. Morais, C. Comminges and K. B. Kokoh, IrO_2 coated on RuO_2 as efficient and stable electroactive nanocatalysts for electrochemical water splitting, *J. Phys. Chem. C*, 2016, **120**, 2562–2573.

57 X. Gao, J. Chen, X. Sun, B. Wu, B. Li, Z. Ning, J. Li and N. Wang, Ru/RuO_2 nanoparticle composites with N-doped reduced graphene oxide as electrocatalysts for hydrogen and oxygen evolution, *ACS Appl. Nano Mater.*, 2020, **3**, 12269–12277.

58 D. Voiry, M. Chhowalla, Y. Gogotsi, N. A. Kotov, Y. Li, R. M. Penner, R. E. Schaak and P. S. Weiss, Best practices for reporting electrocatalytic performance of nanomaterials, *ACS Nano*, 2018, **12**, 9635–9638.

59 C. Liu, H. Ma, M. Yuan, Z. Yu, J. Li, K. Shi, Z. Liang, Y. Yang, T. Zhu, G. Sun, H. Li and S. Ma, $(NiFe)S_2$ nanoparticles grown on graphene as an efficient electrocatalyst for oxygen evolution reaction, *Electrochim. Acta*, 2018, **286**, 195–204.

60 L. Fu, J. Zhou, L. Zhou, J. Yang, Z. Liu, K. Wu, H. Zhao, J. Wang and K. Wu, Facile fabrication of exsolved nanoparticle-decorated hollow ferrite fibers as active electrocatalyst for oxygen evolution reaction, *Chem. Eng. J.*, 2021, **418**, 129422.

61 Y. Li, H. Wang, L. Xie, Y. Liang, G. Hong and H. Dai, MoS_2 nanoparticles grown on graphene: an advanced catalyst for the hydrogen evolution reaction, *J. Am. Chem. Soc.*, 2011, **133**, 7296–7299.

62 H. Wang, L. Ouyang, G. Zou, C. Sun, J. Hu, X. Xiao and L. Gao, Optimizing MoS_2 edges by alloying isovalent W for robust hydrogen evolution activity, *ACS Catal.*, 2018, **8**, 9529–9536.

63 Y. Wang, Z. Liu, H. Liu, N. T. Suen, X. Yu and L. Feng, Electrochemical hydrogen evolution reaction efficiently catalyzed by Ru_2P nanoparticles, *ChemSusChem*, 2018, **11**, 2724–2729.